

ContrasInver: Voxel-wise Contrastive Semi-supervised Learning for Seismic Inversion

Yimin Dou, Timing Li, Kewen Li, Hongjie Duan, Zhifeng Xu

arXiv:2302.06441v1 [physics.geo-ph] 13 Feb 2023

Abstract—Recent studies have shown that learning theories have been very successful in hydrocarbon exploration. Inversion of seismic into various attributes through the relationship of 1D well-logs and 3D seismic is an essential step in reservoir description, among which, acoustic impedance is one of the most critical attributes, and although current deep learning-based impedance inversion obtains promising results, it relies on a large number of logs (1D labels, typically more than 30 well-logs are required per inversion), which is unacceptable in many practical explorations. In this work, we define acoustic impedance inversion as a regression task for learning sparse 1D labels from 3D volume data and propose a voxel-wise semi-supervised contrastive learning framework, ContrasInver, for regression tasks under sparse labels. ConstraInver consists of several key components, including a novel pre-training method for 3D seismic data inversion, a contrastive semi-supervised strategy for diffusing well-log information to the global, and a continuous-value vectorized characterization method for a contrastive learning-based regression task, and also designed the distance TopK sampling method for improving the training efficiency. We performed a complete ablation study on SEAM Phase I synthetic data to verify the effectiveness of each component and compared our approach with the current mainstream methods on this data, and our approach demonstrated very significant advantages. In this data we achieved an SSIM of 0.92 and an MSE of 0.079 with only four well-logs. ConstraInver is the first purely data-driven approach to invert two classic field data, F3 Netherlands (only four well-logs) and Delft (only three well-logs) and achieves very reasonable and reliable results.

I. INTRODUCTION

Oil is called the blood of the industry, recent studies have shown that learning theories have been very successful in hydrocarbon exploration [1]–[8]. Impedance estimation is a critical step in characterizing hydrocarbon reservoirs from exploration data (seismic data) [9]. Current Deep Learning (DL) methods require geologically similar pre-trained models or dozens to even more logs to achieve promising results [10]–[17]. In fact, most new and special oil and gas fields cannot meet this requirement. Furthermore, logging is very expensive, often costing millions to tens millions dollars for a single logged well. Therefore, the use of fewer well-logs to accurately estimate acoustic impedance is of high engineering and economic value to exploration efforts.

Corresponding author: Kewen Li, likw@upc.edu.cn

Yimin Dou, Kewen Li, Zhifeng Xu College of computer science and technology, China University of Petroleum (East China) Qingdao, China.

Yimin Dou: emindou3015@gmail.com

Timing Li, College of Intelligence and Computing, Tianjin University Tianjin, China.

Hongjie Duan, Shengli Oilfield Company, SINOPEC Dongying, China.

This work was supported by grnts from the National Natural Science Foundation of China (Major Program, No.51991365), and the Natural Science Foundation of Shandong Province, China (ZR2021MF082).

Theory-driven inversion is the common means of impedance estimation in traditional hydrocarbon exploration, which includes sparse-based [18]–[20], model-based [21], [22] and other methods [23], [24]. These approaches are more dependent on the initial model and the hyperparameter settings, and here we focus on the learning task of data-driven impedance estimation. Fig. 1 illustrates the seismic-logging correspondence and the data-driven acoustic impedance inversion task.

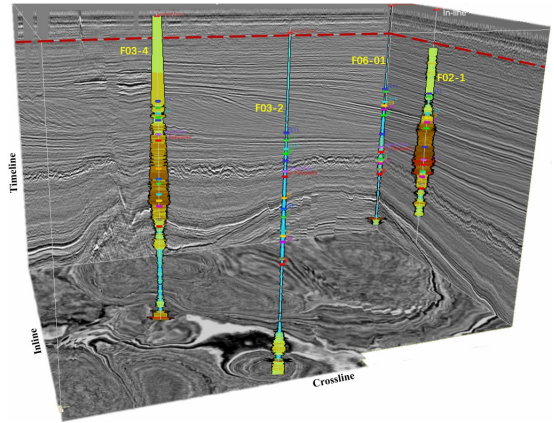


Fig. 1. Data-driven acoustic impedance inversion task. Take F3 Netherlands as an example, the figure shows a complete seismic volume and four well-logs. The seismic volume is three-dimensional, and the size is timeline \times inline \times crossline. The well-log data is one-dimensional, size is $1 \times d_i$ ($d_i \leqslant$ timeline). The four well-logs correspond in position to each of the four 1D seismic traces. The impedance labels in the well-logs are continuous values. In this figure, the data-driven seismic inversion task is to supervise a 3D data volume using four 1D well-logs.

1) *Recent DL methods*: In the beginning, researchers tried to find mapping relationships between seismic traces that matched the logging dimension. Hampson demonstrated that impedance can be predicted by combining multiple seismic traces and corresponding attributes using a simple neural network [25]. Recently an increasing amount of work has started to use DL to estimate impedance [10]–[17]. However, it is well known that DL relies on significant amounts of data, so some of these works use semi-supervised methods. Wu et al. used a semi-supervised method based on adversarial learning [26], [27], a prototype of which was first proposed by Wei [28], who trained the discriminator to distinguish between confidence maps from labeled and unlabeled data predictions. The method depends on having enough labels to ensure the stability of the Generative Adversarial Networks (GAN) [29], so the inversion of the SEAM Phase I (Fig. 4, 7) still requires 34 logging labels, and its predictions have significant discontinuities in the horizontal direction, the same drawback is also reflected

in other semi-supervised impedance inversion methods [30]–[32]. The discontinuity in the horizontal direction is due to the fact that these methods try to match the dimensionality of the logs by downscaling the 3D or 2D seismic data, which is avoided by the multidimensional inversion proposed by Wu et al [11], the idea of this method originates from medical image segmentation [33], where the model is trained using labels of the same dimensionality as the seismic and the weights of the unlabeled regions are set to zero. The method achieved a significant performance improvement with the use of 40 logs in SEAM.

2) *Rethinking DL for impedance inversion*: The deep integration of advanced learning theories and methods with the field of geophysics requires knowledge of both fields and insight into the connections and challenges between them, which is the beauty of the interdisciplinary approach. In this introduction, with Fig 1 we reduce the inversion problem to a task that is very understandable by data scientists, i. e., the regression learning task between 3D data and 1D labels. In the case of very few labels, this task is also very attractive and challenging in the field of machine learning.

Impedance inversion can be defined as a semi-supervised regression learning task. Recent advances in unsupervised and semi-supervised learning can be attributed to the rise of contrastive learning [34], [35], which has now become an important branch in the field of DL [36]. Semi-supervised learning based on contrastive learning emphasizes more on consistency in feature space [37]–[40], while general semi-supervised uses more consistency in label space [41]–[44]. These methods have achieved promising results in both natural and medical images, but they have not been widely promoted and applied in the geophysical field [2], and even less work has been done to combine them with acoustic impedance inversion.

In this work, we present ConstrInver, a voxel-wise contrastive semi-supervised learning inversion framework, for the inversion task of 3D seismic data. ConstrInver-based inversion does not require overly dense well-log labels, and it uses an order of magnitude fewer logs than existing methods to obtain higher quality inversion results, and our contributions are mainly as follows.

- A semi-supervised learning framework and paradigm for seismic inversion is provided, which significantly improves the performance of data-driven inversion and greatly reduces the number of well-logs required.
- A novel pre-training approach for 3D data-driven inversion, which can also be used for non-semi-supervised inversion.
- A semi-supervised learning approach based on contrastive training to diffuse local well-log information to the global.
- Proposes a continuous-valued vectorized characterization approach for contrastive training-based regression tasks.

II. RELATED WORKS

Impedance estimation is a dense voxel-wise regression task, common regression tasks in computer vision are human pose estimation, face counting, etc., but unfortunately we did

not find a generalized semi-supervised learning method for these tasks, this is mainly due to the fact that these tasks have common large-scale datasets and are well generalized. Most dense tasks are currently targeted at image segmentation. Therefore in this section we focus on semi-supervised and contrastive learning image segmentation algorithms, which are more potentially combined with impedance estimation tasks. We summarize some of the most relevant work and analyze the problems and challenges they may bring when applied to impedance inversion.

A. Semi-supervised Learning

Semi-supervision wants to learn from unlabeled data, and creating pseudo-labels is a common approach [45]. Most methods choose high confidence predictions as pseudo-labels [41]–[44], which can also lead to most unlabeled data being discarded due to their unreliability, and some recent work has started to focus on lower confidence prediction values [46].

Existing methods for creating pseudo-labels are suitable for classification and segmentation tasks that employ discrete labels. The target of the regression task is the continuous value, it is not possible to create pseudo-labels based on confidence, and blindly using unfiltered pseudo-labels can degrade model performance [47]. Therefore it is difficult to use such methods in impedance estimation tasks if a reasonable way cannot be found to evaluate the quality of the network output.

Another common approach is the use of GAN [29]. Semi-supervised methods based on GAN have been applied to impedance inversion by some researchers [26], [27], but more often in the field of natural and medical image segmentation [28], [48]–[53]. The earliest use of such methods was by Hung et al. who suggested training discriminators to discriminate between confidence maps of labeled and unlabeled data predictions [28]. Mittal et al. used one branch to perform low entropy predictions using GAN methods and another branch to eliminate false positive predictions using a moving average model [48]. The similar approach has been followed by the work of Feng et al. [50], [51].

Such methods pseudo-labels are not based on confidence but generated by GAN, and GAN-based semi-supervised methods seem to be available for regression tasks. However, it still requires enough labeled data for stable GAN training [28], and it is difficult to provide enough logs in some oil and gas field work areas. The most serious problem of the method is that the GAN training requires complete labeling for each sample, which leads to the method being limited to the training of 1D networks, and the low-dimensional networks lead to significant horizontal discontinuities in the final 3D impedance volume [26], [27]. Lateral discontinuity is a common problem in current data-driven inversion. Wu solves this problem using a multidimensional inversion approach [11], which uses a 2D neural network to learn 1D labels and sets the weight of unlabeled regions to 0. Learning using sparse labels was first proposed in 3D UNet and used in 3D medical image segmentation [33], later applied to geophysical fields such as inversion and fault detection [5], [6], [11].

Finally, consistency regularization, which relies on the model's assumption of invariance to perturbations, i.e., dif-

ferent forms of augmentation done on the same data should produce the same results [54]–[59]. The current consistent regularization generally requires the gradient network to learn from the EMA network, which differs from the approach using pseudolabeling in that it requires consistent features, while the pseudolabeling-based approach requires a consistent distribution of classes.

Consistency regularization methods are almost identical to pseudolabel-based methods in regression tasks, and they face the same dilemma that it is difficult to guarantee that the features learned from the EMA are correct.

B. Contrastive Learning

Self-supervised and unsupervised representation learning has made great strides benefiting from contrastive learning, and these methods migrate information from large-scale datasets to downstream tasks by building pre-trained models [34], [35], [60]. Pixel-level contrastive learning has also been well explored recently, and they are more suitable for tasks such as object detection and semantic segmentation [61]–[63]. In this paper, we expect models to benefit from semi-supervision rather than just building pre-trained models. There is already some work applying this to semi-supervised semantic segmentation [38], [39]. Alonso forces the segmentation network to produce similar pixel-level feature representations for similar samples across the dataset by maintaining a memory bank [38]. Zhong et al. propose a pixel-level negative sampling technique [39]. These methods construct pseudolabels indirectly based on contrastive learning and need to distinguish between positive and negative pairs, which is not realistic for regression tasks.

SimSiam [64] and BYOL [60] demonstrate that contrastive learning can still work without negative pairs by a rational design of the training framework, and PixPro [61] proposes pixel-level contrastive learning with only positive pairs. PixPro calculates the Euclidean distance of pixels in the feature maps of two views after multiple downsampling (encode), determines whether they overlap by setting a distance threshold, and optimizes the cosine similarity of features in the overlapping region, which is perfectly reasonable for representation learning and building pre-trained models. In contrast, semi-supervised learning for segmentation or regression tasks requires the encoded data features to be restored to their original resolution (decode), and the structure of encode and decode is often symmetric, so the effect of optimizing the encoded features is difficult to transfer to the decoder. If the decoded features are optimized, PixPro requires significant memory to compute the distance and similarity matrices at the original resolution, a memory consumption that most hardware cannot afford when working with 3D data, moreover, imperfectly aligned and smoothed features can cause the model to learn inaccurate pseudo-labels. Although these contrastive learning methods are just used to construct pre-trained models, the idea of using only positive pairs still deserves our consideration.

In this paper, we explore the positive pair-only contrast training method, which is equivalent to adding a projection head on the basis of consistent regularization in the semi-supervised learning of regression tasks. We find that the

projection head plays a non-negligible role in this task. In the regression task, the model outputs are continuous values and cannot be trained semi-supervised based on pseudolabeling or consistent regularization. To verify this conclusion, we implemented a regression version of the consistent regularization method, which did not show performance improvements on the pre-trained model, but instead obtained poorer results. When we added the projection head, the semi-supervised learning started to work its magic and the performance showed a very significant improvement, and we explored and improved it further based on that conclusion.

III. APPROACH

In this section, we detail the various components of ConstraInver, which include ContrasInver Pre-train, Log Information Diffusion, Distance TopK Sampling, Vectorized Characterization of Regression, and how they contribute. The overall approach is shown in Fig. 2.

The backbone network uses HRNet [65], replaces the 2D convolution with 3D, the base width is 24, and removes stage 4 (a module with four scales). Backbone is not critical, it can be replaced with any network of fully convolutional autoencoder structures.

A. ContrasInver Pre-train

In this subsection we introduce a novel 3D inversion training method using its role ConstraInver pre-training, which we name ConstraInver Pre-train (CIPT).

In impedance inversion, the value of impedance is highly correlated with its depth (coordinates of Timeline axis) in the seismic data, and ROIs with the same structure or texture may be completely opposite because of their different locations, which is mainly caused by the low-frequency velocity constraint of the seismic. For this reason, current data-driven impedance inversions have input data that retains the full timeline information. These methods require a large number of logs to ensure sufficient training data to prevent overfitting, additionally, these 1D or 2D models yield results with significant lateral discontinuities.

Therefore CIPT was created, which still retains the full information of timeline, i.e., only the inline and crossline are randomly cropped and used as input training data. The random cropping region (this refers to the cropped data, denoted by \mathcal{X}_k) must contain the well-logs to ensure that each sample has supervised information. Suppose the well coordinates are $p_i^{\text{raw}}, p_x^{\text{raw}}$, and the height and width of the sample are s_i, s_x , respectively, then the starting coordinates (upper left coordinates) of the sample are $p_{si}^{\text{raw}}, p_{sx}^{\text{raw}}$, and the range of $p_{si}^{\text{raw}}, p_{sx}^{\text{raw}}$ is expressed as equation (1).

$$\begin{cases} p_{si}^{\text{raw}} \in [p_i^{\text{raw}} - s_i + \tau, p_i^{\text{raw}} + s_i - \tau] \\ p_{sx}^{\text{raw}} \in [p_x^{\text{raw}} - s_x + \tau, p_x^{\text{raw}} + s_x - \tau] \end{cases} \quad (1)$$

where τ is the sample random bound set to ensure that subsequent semi-supervised training can have sufficient overlapping volume, in this paper, $\tau = 4$.

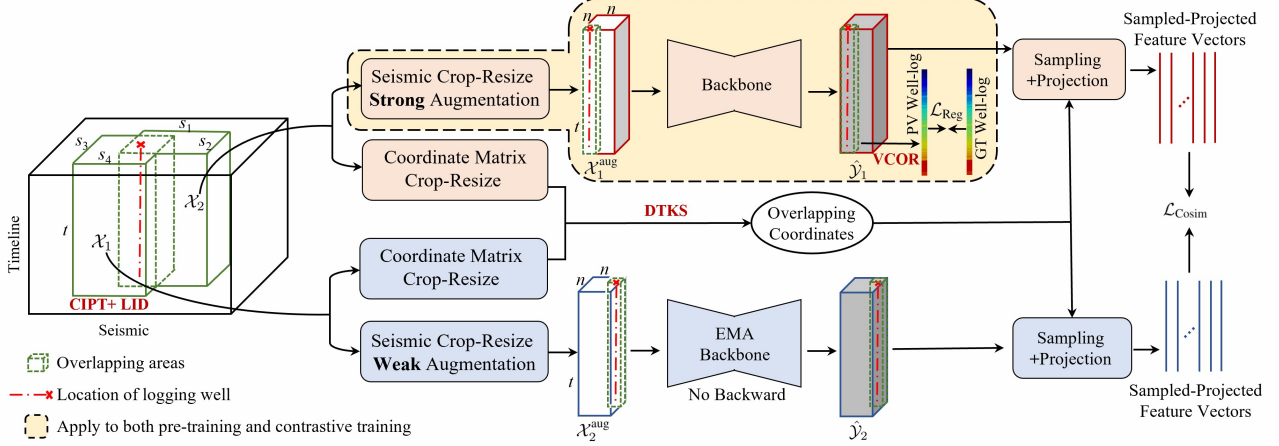


Fig. 2. Where s_k is the uniform distribution of $s_i \in [0.5n, 2n] \cap \mathbb{Z}$, t is the original timeline length, and crop gets each original sample of size $t \times s_i \times s_x$, which is later interpolated to $t \times n \times n$. When calculating losses, only the logging locations are calculated and propagated. \mathcal{L}_{Reg} is regression loss and $\mathcal{L}_{\text{Cosim}}$ is cosine similarity loss i.e. contrastive loss. Backbone is updated by gradient, momentum backbone is updated by equation 4.

Moreover, each cropped sample needs to be interpolated to the same size and data augmentation¹. (denoted by $\mathcal{X}_k^{\text{aug}}$). We set the size of each $\mathcal{X}_k^{\text{aug}}$ to $t \times n \times n$, where n is the length of inline and crossline after resize and t is the timeline size of the original seismic data. To make sure that the interpolated seismic voxels are not severely distorted, we restrict the length of \mathcal{X}_k inline and crossline i.e., $s_k \in \mathcal{S}$, $\mathcal{S} = [\omega \times n, n/\omega] \cap \mathbb{Z}$, where s_k is the original sampling inline or crossline length, \mathcal{S} is the matrix composed of s_k , $\omega = 0.5$. The adjustment of the interpolated well-log coordinates is expressed by the equation 2.

$$\begin{cases} p_i = p_i^{\text{raw}} n / s_i \\ p_x = p_x^{\text{raw}} n / s_x \end{cases} \quad (2)$$

where p_i, p_x are the adjusted logging coordinates and $p_i^{\text{raw}}, p_x^{\text{raw}}$ are the coordinates before sampling. It should be noted that $n = 48$ for training in this paper, because the backbone is chosen as a full convolutional network, so the inference can be of any cube size. The pre-trained part has been indicated in Fig. 2. Where this pre-training uses \mathcal{L}_1 regression loss. In the calculation of the loss, it is the 1D logging labels that supervise the 3D seismic volume data, and the basic principle is to calculate the loss of the well location only, which can be expressed by the equation 3. Due to the shared parameter mechanism of convolution, the absent labels do not affect the training of the model. This training approach using sparse labels was first mentioned by Çiçek et al. [33].

$$\begin{aligned} \mathcal{L}_{\text{Reg}} &= \sum_{d=1}^t \sum_{h=1}^n \sum_{w=1}^n \mathcal{M}_{d,h,w} \|\hat{y}_{d,h,w} - y_{d,h,w}\|_1 \\ \mathcal{M}_{d,h,w} &= \begin{cases} 1, & \text{well location} \\ 0, & \text{not well location} \end{cases} \end{aligned} \quad (3)$$

In contrast to existing methods, we are able to obtain various training data without relying on a large number of well-logs, this method requires only one label to obtain $\mathcal{S} \cdot \mathcal{S}^T$.

¹See below for data augmentation methods

(Kronecker product) different samples, and since our input is 3D, it is guaranteed to be continuous in all directions. More importantly, the method sets the stage for the contrastive learning that follows. CIPT can also be used for other non-semi-supervised data-driven inversion training, and the results of training using only CIPT are shown in experiments where it still outperforms most existing methods.

B. Contrastive semi-supervised learning

The framework follows a dual-network asymmetric structure, where the backbone branch updates parameters by gradient and the Exponential Moving Average (EMA) backbone updates via equation (4).

$$\mathcal{V}_t^{\text{ema}} = \lambda \mathcal{V}_{t-1}^{\text{ema}} + (1 - \lambda) \mathcal{V}_t \quad (4)$$

Where $\mathcal{V}_t^{\text{ema}}$ is the EMA backbone parameter for the current moment (step), $\mathcal{V}_{t-1}^{\text{ema}}$ is the EMA backbone parameter for the previous moment, and \mathcal{V}_t is the backbone parameter for the current moment, λ is the momentum weight, which satisfies the equation (5),

$$\lambda = 1 - 0.05 \times (\mathbf{F}_{\text{cos}}(\pi \mathcal{I}_{\text{cu}} / \mathcal{I}_{\text{all}}) + 1) / 2 \quad (5)$$

\mathcal{I}_{all} is the total number of steps to be trained, \mathcal{I}_{cu} is the current step.

The proxy task of this framework is based on the fact that the overlapping regions of two views (cropped samples, \mathcal{X}_k or $\mathcal{X}_k^{\text{aug}}$) in seismic data should have exactly the same impedance values. Although a similar idea has been used for pre-training of dense image tasks [61]. However, as described above (II-B), its use for the semi-supervised regression task of 3D models still needs to overcome many difficulties and the potential for this task needs to be further developed.

1) *Log Information Diffusion*: In this subsection, we introduce the log information diffusion method (LID) in ConstalInver, which broadcasts the local log information to the global seismic volume by semi-supervised learning, thus accomplishing high-quality inversions under extremely sparse logs.

In III-A we detailed the pre-training process, which spreads the single log information to the local region of the seismic, the size of which depends on the extent of \mathcal{S} . LID can further broadcast the local information to the global seismic volume.

LID achieves information diffusion by creating virtual well locations. The virtual well location is obtained by doing a random offset to the real well location, the offset is gradually expanded with training, and the same sample crop approach is executed by the virtual well location so that the crop location is gradually diffused outward. The random offset is denoted by α_i, α_x , with α_i, α_x taking a range of values that grows linearly with the number of training steps, as defined in equation (6).

$$\begin{cases} \alpha_i \in [-\varphi \mathcal{I}_{cu}/\mathcal{I}_{all} \times l_i/2, \varphi \mathcal{I}_{cu}/\mathcal{I}_{all} \times l_i/2] \\ \alpha_x \in [-\varphi \mathcal{I}_{cu}/\mathcal{I}_{all} \times l_x/2, \varphi \mathcal{I}_{cu}/\mathcal{I}_{all} \times l_x/2] \end{cases} \quad (6)$$

where \mathcal{I}_{all} is the total number of steps to be trained, \mathcal{I}_{cu} is the current step, l_i and l_x are the inline and crossline lengths, respectively, and α_i and α_x are the range of offsets on the inline and crossline, respectively, φ is a parameter controlling the termination of diffusion, that is, when the training reaches $1/\varphi$, the diffusion is terminated, and then virtual wells are randomly set in the entire seismic volume and samples are generated, in this paper, $\varphi = 2$. The coordinates of the virtual well (p_i^{virt}, p_x^{virt}) can be expressed as the equation (7).

$$\begin{cases} p_i^{virt} = p_i^{raw} + \alpha_i \\ p_x^{virt} = p_x^{raw} + \alpha_x \end{cases} \quad (7)$$

Each well is randomly generated by two views (samples) in the manner described by III-A. This method of generating samples ensures that the two have at least the overlapping volume of $4\tau^2 t$.

The LID needs to calculate the Euclidean distance between the center coordinates of two views and the well coordinates, and the farther distance is noted as \mathcal{X}_1 , which performs strong augmentation to get \mathcal{X}_1^{aug} , and the closer distance is noted as \mathcal{X}_2 , which performs weak augmentation to get \mathcal{X}_2^{aug} . Weak augmentation includes only coordinate transformations such as interpolation, random rotation and mirroring. Strong augmentation includes random noise and random gamma transformations in addition to coordinate transformations. It is worth mentioning that we interpolate the timeline direction in addition to the inline and crossline directions. Unlike the other two directions, because the integrity of the information in the timeline direction and the trainability of the model are guaranteed at the same time, the interpolation of the timeline direction is performed at the scale of the batch, i.e., the interpolation of the same multiplicity is performed for the timeline direction of a whole batch, and the interpolation range is $t_r \in [\omega \times t, t/\omega]$. The timeline direction needs to be resized back to the original length t after passing through the network output to ensure that the subsequent steps proceed smoothly.

Feed \mathcal{X}_1^{aug} into backbone and \mathcal{X}_2^{aug} into EMA backbone to get \mathcal{Y}_1 and \mathcal{Y}_2^{ema} . The vector pairs in the overlapping regions of \mathcal{Y}_1 and \mathcal{Y}_2^{ema} are extracted by the DTKS proposed by III-B2,

and then the projected feature vectors are made closer using cosine similarity (8).

$$\mathcal{L}_{cosim}(v_1, v_2^{ema}) = \frac{v_1 \cdot v_2^{ema}}{\max(\|v_1\|_1 \cdot \|v_2^{ema}\|_1, \epsilon)} \quad (8)$$

where ϵ is a small value to avoid dividing by 0, v_1 and v_2^{ema} are the feature vectors of the overlapping regions after MLP projection. The difference between this process and consistency regularization is that we do not require exact consistency of features or outputs, LID emphasizes backbone outputs with consistent direction after projection of feature vectors. In this regard LID is characterized by contrastive learning, and this feature consistency approach is important in that it also plays a semi-supervised role in ConstraInver, hence it is called contrastive semi-supervised learning. We experimentally demonstrate that the performance of projected feature consistency is significantly higher than that of unprojected and label consistency, which we hypothesize is due to the filtering effect of the projection head on meaningful information [66], [67].

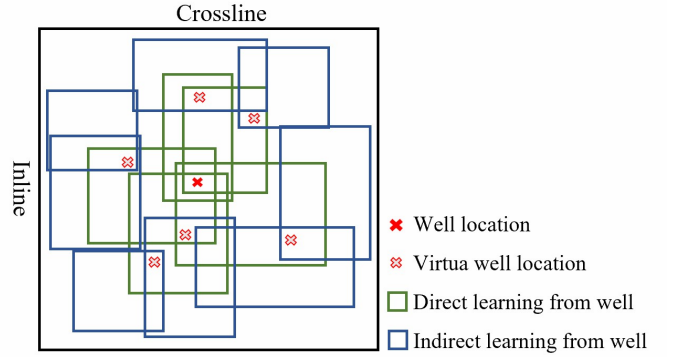


Fig. 3. LID process. The virtual well locations are generated by adding residuals to the well locations and gradually spread outward, with the resulting outer circle views learning from the inner circle through overlapping regions and EMA backbone.

We include at least one sample containing real wells in each batch to ensure that the learning process does not deviate from the right track. Thus for each batch, the final loss function can be expressed as the equation (9).

$$\mathcal{L}_{LID} = \eta_1 \mathcal{L}_{reg} + \eta_2 \mathcal{L}_{cosim} \quad (9)$$

where η_1 and η_2 are weight parameters, let $\eta_1 = 1$ and $\eta_2 = 10$.

Fig 3 illustrates the process of LID, in this figure, the inner circle view learns impedance information directly from the logs, and the knowledge learned by the model gradually accumulates in the EMA backbone as diffusion proceeds. The outer circle view can also learn the impedance information indirectly through the overlapping area with the inner circle view and the EMA backbone.

2) *Distance TopK Sampling*: In the previous subsection, we mentioned the need to calculate the cosine similarity loss of the features in the overlapping region of two views, and the key step is to find the coordinates of the one-to-one correspondence between the two overlapping regions, which

intuitively seems not difficult, but the input view needs to be interpolated, randomly mirrored and randomly rotated, among which the interpolation is the most drastic change in coordinates, and it will completely disrupt the one-to-one correspondence of the original view. Therefore, calculating the correspondence between the overlapping areas in the two views after augmentation is the basis for ensuring that the frame works.

The method of PixPro is to calculate the one-to-one corresponding distances of two view coordinates and the cosine similarity loss of the projection vectors simultaneously during forward propagation to obtain the distance matrix and the similarity loss matrix, and to generate a mask by setting the threshold on the distance matrix, the position where the distance is below the threshold is the overlap position, this obtains the binary matrix and applying it to the similarity matrix. Calculating the distance matrix and similarity matrix can be expressed as equations (10) and (11).

$$\mathcal{A}_{\text{dist}} = \mathcal{P}_1^T \cdot \mathcal{P}_2 \quad (10)$$

$$\mathcal{A}_{\text{cosim}} = \mathcal{L}_{\text{cosim}}(\mathcal{F}_1^T \cdot \mathcal{F}_2) \quad (11)$$

where $\mathcal{P}_1, \mathcal{P}_2$ are the flattened coordinate matrices of view1 and view2 respectively (length is $w \times h$, w, h are the width and height of the feature map respectively), $\mathcal{F}_1, \mathcal{F}_2$ are the flattened feature maps of view1 and view2 respectively, the length of each element in \mathcal{F} depends on the MLP projection and is typically 128. Equation (10) has a time complexity of $O(n^3)$ and (11) is $O(m^3 n^3)$.

When equations (10) and (11) are applied to an overly downsampled image, there is no significant computational or memory occupation, e.g., PixPro downsamples an image of size 224×224 by a factor of 32 to obtain a 7×7 feature map, where the lengths of $\mathcal{P}_1, \mathcal{P}_2$ and $\mathcal{F}_1, \mathcal{F}_2$ are 49. However, the situation becomes complicated when we apply it to unsampled 3D data. As in Fig. 2's framework, when $n = 48$ and $t = 400$, the length of \mathcal{P} and \mathcal{F} becomes $48 \times 48 \times 400 = 9.22 \times 10^5$. When the time complexity is $O(m^3 n^3)$, $m = 128, n = 9.22 \times 10^5$, most GPUs cannot afford the resulting memory footprint and computational effort. Because our method does not sample the timeline direction, the coordinates of all samples in the timeline are the same. In this case, the complexity of computing the coordinates and the similarity loss matrix is the same as that of the non-downsampled 2D data, and the length of \mathcal{P} and \mathcal{F} is $48 \times 48 = 2304$, which is also an unnecessary computational overhead that not only affects the batchsize setting, but also greatly reduces the training speed.

The reason why the method mentioned above calculates the whole feature map point-to-point distance and feature similarity is because it needs to ensure that each sample in the batch of the input network has the same dimensionality and size. This is well ensured by setting a combination of threshold and mask, but also brings a lot of unnecessary computation, such as the similarity of regions outside the distance threshold, which takes up more than 90% of the computational resources for this step. Therefore, we propose Distance TopK

Sampling (DTKS), which completely eliminates the burden of computing overlapping regions on the GPU, allowing us to train the network with a larger batchsize and at a faster speed.

DTKS still needs to calculate the distance matrix $\mathcal{A}_{\text{dist}}$, which is much simpler than the similarity matrix $\mathcal{A}_{\text{cosim}}$, but it still consumes high graphics memory, so we suggest moving the process to the CPU and calculating $\mathcal{A}_{\text{dist}}$ at the same time as the \mathcal{X}_1 and \mathcal{X}_2 augmentations, the specific process is as follows.

First establish the coordinate matrix \mathcal{C}_m , the height and width of \mathcal{C}_m are the inline and crossline lengths of the seismic data respectively, each element of the matrix is the coordinates of the current position. When \mathcal{X}_1 and \mathcal{X}_2 are obtained by cropping the seismic data, \mathcal{C}_m is obtained at the same position of \mathcal{C}_1 and \mathcal{C}_2 . The \mathcal{X}_1 and \mathcal{X}_2 are augmented with coordinate transformations such as random mirroring, random rotation and resize (bilinear interpolation) to obtain $\mathcal{X}_1^{\text{aug}}$ and $\mathcal{X}_2^{\text{aug}}$, and \mathcal{C}_1 and \mathcal{C}_2 also perform the same coordinate augmentation and flattening to obtain \mathcal{P}_1 and \mathcal{P}_2 . The distance matrix is obtained by equation (10).

\mathcal{P}_1 and \mathcal{P}_2 experience the bilinear interpolation operation, and the original overlap region is slightly shifted, so that elements equal to or close to zero in $\mathcal{A}_{\text{dist}}$ represent overlap positions. To make the size of each sample in the batch consistent, we used TopK sampling and recorded the coordinates of the minimum \mathcal{K} values from $\mathcal{A}_{\text{dist}}$ in $\mathcal{X}_1^{\text{aug}}$ and $\mathcal{X}_2^{\text{aug}}$, respectively. \mathcal{K}, τ and ω must satisfy the equation (12),

$$\mathcal{K} \leq (2\tau\omega)^2 \quad (12)$$

in this paper, $\tau = 4, \omega = 0.5$, we set $\mathcal{K} = 16$.

The above operations are done at the CPU. We apply the recorded overlapping coordinates to the feature maps output by backbone and EMA backbone, respectively, to obtain $t \times \mathcal{K}$ pairs of feature vectors. And the subsequent MLP and cosine similarity loss are computed only for these feature vectors, without computing other non-overlapping regions.

DTKS only needs to calculate the projection and cosine similarity of $t \times \mathcal{K}$ on the overlapping positions while preserving the consistency of the sample sizes within the batch, which greatly saves the computational resources of the GPU. Not only that, given the current limitations of most GPU graphics memory, DTKS is arguably the only option when handling overlapping regions of high resolution or undersampled images.

3) *Vectorized Characterization of Regression*: In general the regression task requires weighting the feature vectors of the final layer from the backbone to obtain the regression values, this way a weighting layer needs to be trained in addition to the backbone. The above section details the part where we train the backbone using LID and regression, where the weighting layer can be effectively trained by regression loss, but LID does not take care of the weighting layer.

Using only a very limited number of logs for training may result in a weighting layer that does not generalize effectively and may even introduce low quality gradients to the backbone. One solution that readily comes to mind is to change the optimization objective of LID to the final regression value, i.e., to discard equation (8) and replace it with the commonly used \mathcal{L}_1

or \mathcal{L}_2 regression loss to directly optimize the weighting layer. However, this degrades the model to consistent regularization, and as mentioned in related work, such methods are suitable for classification and segmentation tasks, and inevitably cause the model to learn the wrong information when it is applied to regression. In experiment (Fig. 6 (g) (o), Tabel II), we confirmed that this idea is not work in impedance regression, and it leads to obtaining worse models than pre-trained ones. And it is clear from ablation experiment (Fig. 6, Tabel II) that even though LID does not act directly on the weighting layer, its improvement on the performance of the pre-trained model is significant, so if the backbone output feature map results are used directly as regression results, the problem of having to train the weighting layer is evaded, however, the output impedance must be single channel and we still need to weight the last layer feature map without parameters, the most intuitive way is to average, another is our proposed Vectorized Characterization of Regression (VCOR).

VCOR uses the cosine of the feature vector and the basis vector as the final impedance value, and its optimization objective is the direction of the vector in the feature space, which avoids the numerical compulsion and uniqueness of the optimization objective. LID uses cosine similarity loss, which makes the overlapping region feature vectors oriented in the same direction, which is consistent with the optimization objective of VCOR. The final impedance value can be expressed as equation (13),

$$\mathbf{F}_{\text{cosim}}(\hat{v}, v_{\text{base}}) = \frac{\hat{v} \cdot v_{\text{base}}}{\max(\|\hat{v}\|_1 \cdot \|v_{\text{base}}\|_1, \epsilon)} \quad (13)$$

where v_{base} is base vector, we choose to use the one vector, i.e., $[1, 1 \dots 1]$. The loss function of VCOR is represented by the equation (14),

$$\mathcal{L}_{\text{VCOR}} = \sum_{d=1}^t \sum_{h=1}^n \sum_{w=1}^n \mathcal{M}_{d,h,w} \|\mathbf{F}_{\text{cosim}}(\hat{v}_{d,h,w}, v_{\text{base}}) - y_{d,h,w}\|_1$$

$$\mathcal{M}_{d,h,w} = \begin{cases} 1, & \text{well location} \\ 0, & \text{not well location} \end{cases} \quad (14)$$

compared to the equation (3), it just replaces $\hat{y}_{d,h,w}$ to $\mathbf{F}_{\text{cosim}}(\hat{v}_{d,h,w}, v_{\text{base}})$.

IV. EXPERIMENTS

In this section, we first performed an ablation study on synthetic data to verify the effectiveness of each component of ContrasInver. Then a comparison with current mainstream methods is performed to verify the advanced nature of ContrasInver. Finally, two surveys, F3 Netherlands (F3) and Delft, were inverted. These two surveys provide only four and three available impedance logs, respectively. Although these two surveys are very classical and have been applied to a large number of studies, to our knowledge, no one has yet used machine learning methods to invert these two surveys, probably because the number of logs has limited the researchers' exploration of these two surveys.

A. Ablation Experiments

1) *Dataset*: The ablation study uses the 3D velocity synthetic model SEAM Phase I, the advantage of synthetic data is its complete 3D ground truth, which facilitates the quantitative and qualitative validation of the performance of various methods. This data contains a complex salt body and the impedance values show a dramatic variation from the surrounding layer to the salt body, with lateral and vertical impedance variations also observed in the surrounding layer [11]. Its original size is $600 \times 501 \times 502$ (timeline, inline, crossline), for the convenience of training and inference, we resize it to $400 \times 501 \times 502$ (timeline, inline, crossline). This data was denoised, which are shown in Fig 4.

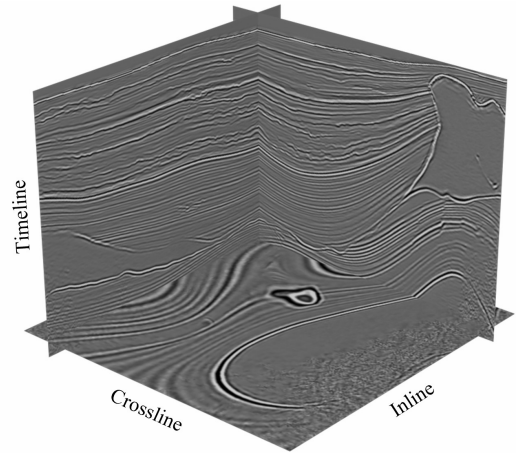


Fig. 4. This figure shows the SEAM Phase I profile in grayscale.

For SEAM Phase I, current methods often use 30 or more logs [11], [12], while we have reduced this number to 4 or 9 and achieved better performance. Our experiments were performed on 4 and 9 logs, and Fig. 5 has marked the training and validation logs.

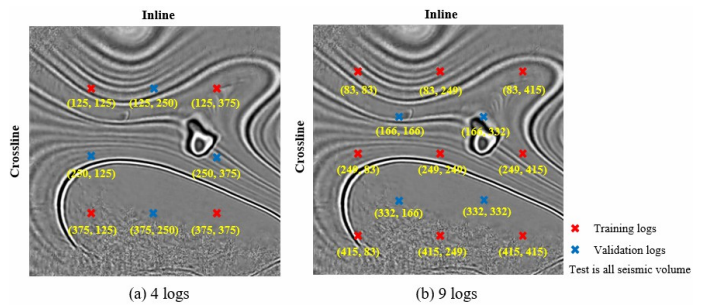


Fig. 5. The training and validation logs have been marked in the figure, since the number of training and validation logs is insignificant in the whole seismic volume, the test set is the whole seismic volume. As indicated in figure, we used equally spaced log sampling, which is to ensure that the selection of well locations should be representative and fair in the case of a extremely limited number of logs.

2) *Hyperparameter setting*: G_1 iterates 55000 steps and the other groups perform 5000 steps of pre-training and 50000 steps of semi-supervised training. All training was performed using the AdamW [68] optimizer with a learning rate of 0.001. The training was performed on two 3090Ti with a batchsize

of 6. The model used for the test set is the best performer on the validation set. The hyperparameter settings for the ablation experiment are shown in Table I.

TABLE I
HYPERPARAMETER SETTING

CIPT	Projection head	LID	VCOR
G_1	✓	✗	✗
G_2	✓	✗	✓
G_3	✓	✓	✗
G_4	✓	✓	✗
G_5	✓	✓	✗
G_6	✓	✗	✗
G_7	✓	✓	✓

G_1 is used as a baseline model to perform pre-training only (CIPT); G_2 without projection head, the use of projection head in contrastive learning is not novel, but as mentioned above, the projection head acted as a filter during the semi-supervised learning of the regression task, and compared to groups using the projection head, it is possible to verify that it is effective in providing the backbone with the most valid information and filtering out the wrong information. G_2 is equivalent to the VCOR variant of G_6 , which is also a consistent regularization semi-supervised approach.; G_3 randomly generates virtual wells in the seismic data to obtain sample pairs, it is used to verify the validity of the LID; G_4 without VCOR, instead uses a perceptron to weight the backbone output and then uses L_1 loss for training; G_5 without VCOR, instead, the final features are averaged and then trained using L_1 loss; G_6 supervised process does not use VCOR, instead it uses a perceptron to weight the backbone output, and the semi-supervised process uses label consistency, i.e., it uses L_1 to close the distance between the EMA backbone and the backbone final output impedance values. G_6 is equivalent to achieving consistent regularization of the regression version; G_7 uses the full Constrainer.

3) *Ablation study results:* Table II shows the quantitative results of the experiment, Fig. 6 shows the qualitative results. In Table II, we used three metrics, MSE, MAE and SSIM [69], MSE and MAE to evaluate the numerical difference and distance between the predicted and GT, and SSIM to evaluate the structural difference between the predicted impedance body and the GT. Where MSE is calculated based on the original impedance and SSIM is calculated based on the normalized impedance.

Using only our proposed pre-training method CIPT, G_1 shows results without the assistance of any semi-supervised framework, demonstrating some impedance prediction capability with nine logs, but when the number of logs is reduced to four, G_1 becomes overwhelming.

From the quantitative metrics in Table II, G_2 achieves more outstanding performance in the seven sets of experiments. However, in Fig. 6, the results of G_2 almost obliterate the high impedance region and the entire output is very smooth. This shows that removing the projection head is not desirable in the

TABLE II
ABLATION EXPERIMENT QUANTITATIVE RESULTS

Metrics	4 logs			9 logs		
	MSE	MAE	SSIM	MSE	MAE	SSIM
G_1	0.11419	0.15113	0.88649	0.05117	0.11461	0.90410
G_2	0.07866	0.12803	0.91215	0.03033	0.09433	0.94002
G_3	0.11151	0.12589	0.91180	0.02639	0.07792	0.93750
G_4	0.07478	0.12858	0.91147	0.03692	0.14412	0.94036
G_5	0.13017	0.19576	0.89342	0.03066	0.11212	0.90834
G_6	0.67897	0.55822	0.67252	0.08640	0.14232	0.90791
G_7	0.08734	0.11054	0.91332	0.02692	0.06194	0.94059

regression task. In addition G_2 can be seen as a consistency regularization method where the consistency target is the angle with the basis vector.

G_3 verified the efficacy of LID compared to G_7 . G_4 uses the common combination of perceptron and L_1 loss to output the final impedance value, which has significant distortion. G_5 differs from G_4 in that the perceptron is replaced by the vector mean, which also exhibits lower performance. In regression tasks, the final output is a continuous value, which usually comes by weighting the output of backbone via the perceptron, and is therefore sensitive to the size of the backbone output value. In contrast, in classification or segmentation tasks, after weighting, it is usually normalized nonlinearly using sigmoid or softmax, so it is not sensitive to the size of the backbone output value. Contrastive learning usually optimizes the direction of the backbone, simple numerical weighting in the regression task can nullify the efforts made by contrastive learning. The VCOR vectorizes the output values of the regression model to resolve the contradiction between the contrastive learning and regression tasks, and therefore can obtain better results.

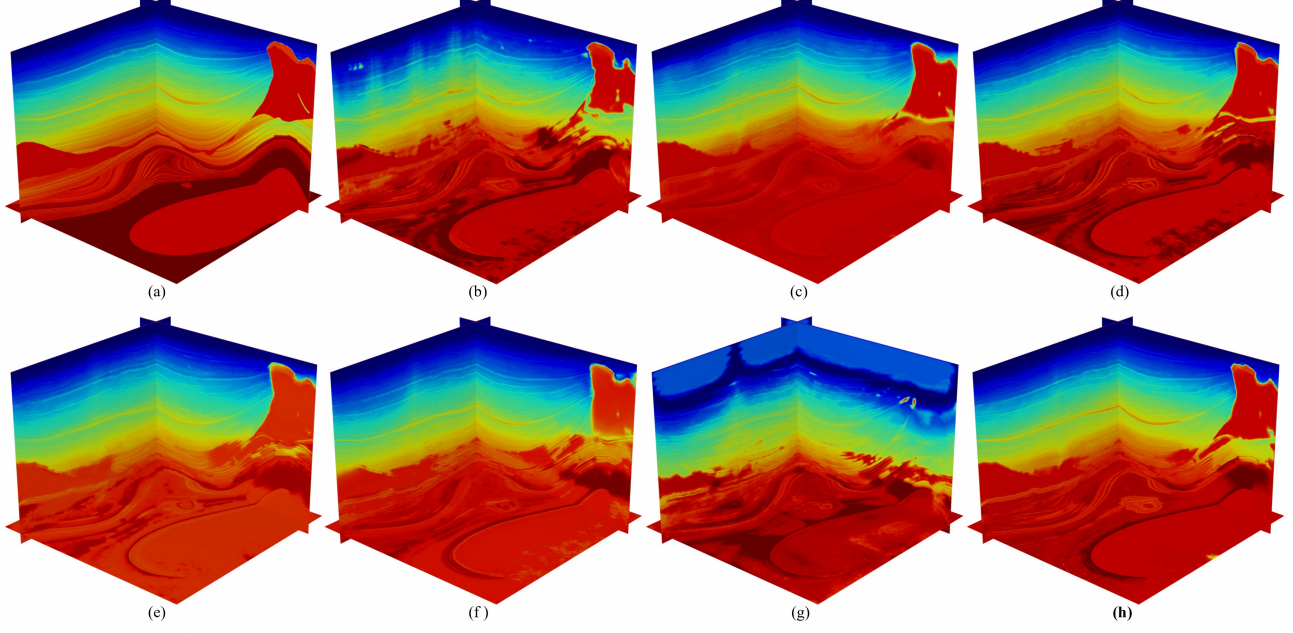
The reason for the lower performance of G_4 and G_5 is the non-uniformity of the optimization objectives of contrastive learning and regression learning, while VCOR unifies the optimization objectives by vectorizing the impedance values, while G_6 is equivalent to changing the optimization vector to the values of the optimization output, and G_6 is also equivalent to achieving consistent regularization of the regression version. As mentioned in the introduction, in the regression task, the pseudolabel-based approach is implemented in the same way as the consistency regularization approach, and in G_6 , unfiltered consistency or pseudolabeling has disastrous consequences and its performance is even lower than that of G_1 .

Although this is an ablation study, it also demonstrates that the currently widely used consistent regularization and pseudolabeling methods are difficult to work in regression tasks. This experiment demonstrates the effectiveness of our proposed individual components while also verifying the usefulness of the projection head, which, in terms of experimental results, can filter invalid or erroneous information during semi-supervised learning.

B. Comparison Experiments

There are widely used 1D CNN-based and semi-supervised methods for adversarial learning based on 1D CNN that are currently available, unfortunately, most of these methods are

Results of training via 4 logs:



Results of training via 9 logs:

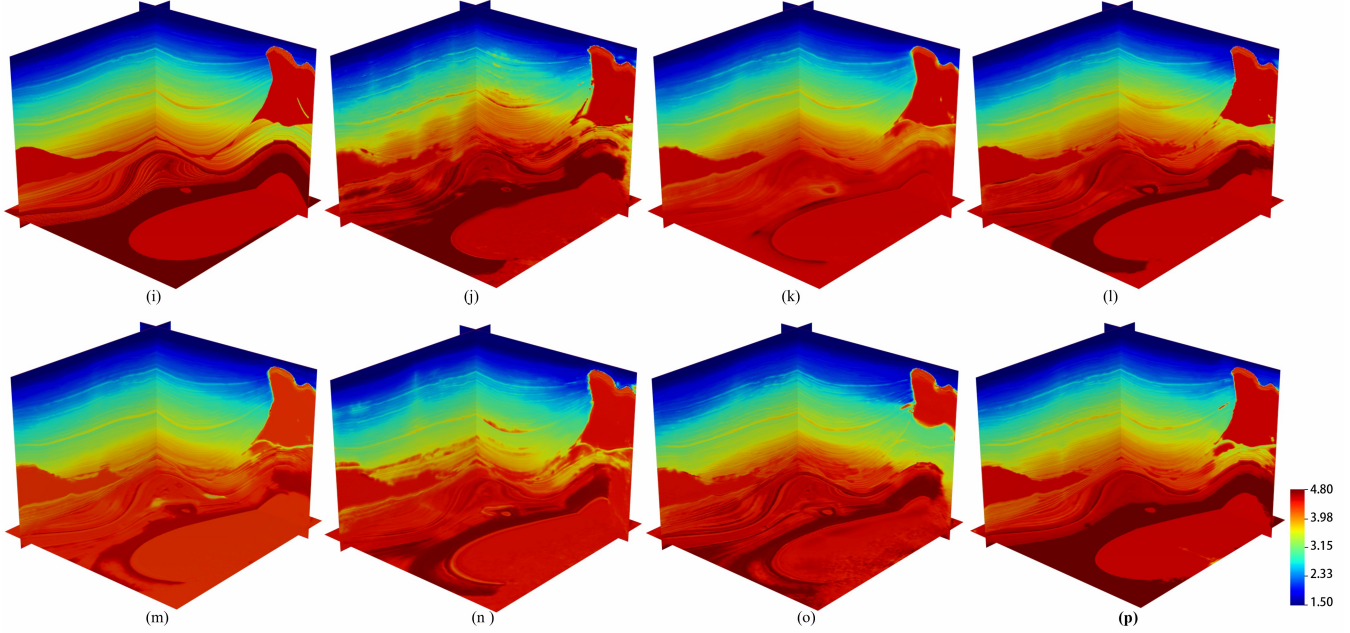


Fig. 6. (b)-(h) training with 4 logs, (j)-(p) training with 9 logs. (a) Ground truth. (b) G_1 training via 4 logs. (c) G_2 training via 4 logs. (d) G_3 training via 4 logs. (e) G_4 training via 4 logs. (f) G_5 training via 4 logs. (g) G_6 training via 4 logs. (h) G_7 training via 4 logs. (i) Ground truth. (g) G_1 training via 9 logs. (k) G_2 training via 9 logs. (l) G_3 training via 9 logs. (m) G_4 training via 9 logs. (n) G_5 training via 9 logs. (o) G_6 training via 9 logs. (p) G_7 training via 9 logs

not open source, and we have implemented three representative works based on the literature [10], [13], [26].

Among them Vishal's work [10] is open source and we reimplemented it using Pytorch with reference to its code and papers, then we added residual structure to further improve the performance, similar methods are also compared in literature [11]. Since its structure is autoencoder, we name it ResNet-AE in the following. Based on this we refer to Wu's work adding attention structure to implement the literature [13], in the following it is named ResANet-AE. We also implemented a

GAN-based semi-supervised method that references the work of Wu [26] and Wei [28], the code uses Wei's and modifies it with reference to Wu's work, In the following it is named Semi-GAN. The CIPT that participated in the comparison experiment is G_1 in Table II, i.e., using only our proposed pre-training method.

Considering that none of the methods involved in the comparison considered the training problem in the case of a few logs, this experiment only compares the case of more than 9 logs. The experiments were still performed on SEAM Phase

I. The original profiles presented by the qualitative experiments are shown in Fig. 7. In this experiment, we used up to 49 well-logs in order to find the upper limit of what can be achieved by the 1D-CNN that is currently widely used for inversion, and all the well-logs in the experiment were sampled equally as shown in Fig. 5.

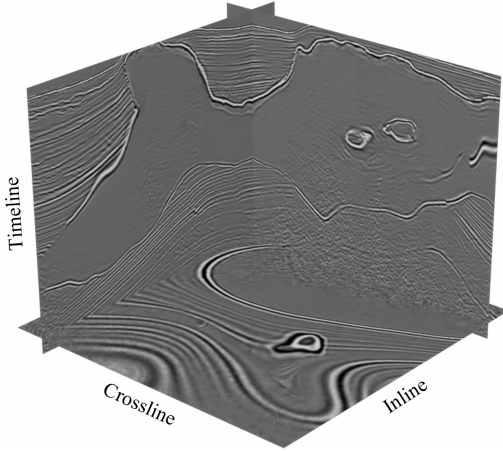


Fig. 7. This figure shows the SEAM Phase I profile in grayscale.

1) *Hyperparameter setting*: The CIPT method was iterated 55000 steps, ConstraInver was pre-trained with 5000 steps and semi-supervised training with 50000 steps, and the other methods were iterated 55000 times. Using the AdamW optimizer, the learning rate is 0.001. The training was performed on two 3090Ti with a batchsize of 6. The model used for the test set is the best performer on the validation set.

TABLE III
COMPARISON EXPERIMENT QUANTITATIVE RESULTS

<i>Methods</i>		<i>MSE</i>	<i>MAE</i>	<i>SSIM</i>
4 logs	CIPT	0.11419	0.15113	0.88649
	ContrasInver	0.08734	0.11054	0.91332
9 logs	ResNet-AE	0.22849	0.22775	0.69492
	ResANet-AE	0.16949	0.18451	0.78019
	Semi-GAN	0.16962	0.20201	0.73196
	CIPT	0.05117	0.11461	0.90410
	ContrasInver	0.02692	0.06194	0.94059

2) *Comparison experiment results*: All three 1D-CNN-based methods in Fig. 9 (b-d) show poor performance because 1D-CNN loses lateral information, resulting in a significant horizontal discontinuity. The same conclusion can be obtained in the quantitative experiments in Table III. The advantage of 1D-CNN over our method is the faster training speed, which takes about 20 minutes to train a usable model on 3090Ti, while our method takes more than 10 hours.

To further explore the upper limit of what can be achieved by this widely used method for impedance inversion, we gradually increased the number of logs to 49. Fig.8 (g-j) shows the variation of the qualitative results of ResNet-AE with the increase in the number of logs. Fig. 9 shows the variation of quantitative results of the three 1D-CNN-based methods, ResNet-AE, ResANet-AE and GAN-Semi, with the increase of the number of logs.

These experiments demonstrate that the 1D-CNN has obvious limitations, because no lateral correlation is considered, resulting in a significant discontinuity in its laterality. In comparison with the 3D-Pretrain method without semi-supervised learning, the quantitative metrics are only equal to the results of the method using nine logs when the number of logs is increased to more than 36. In the comparison with ContrasInver, even when the number of logs was increased to 49, these methods were unable to achieve the performance achieved by ContrasInver using nine logs. Comparative experiments show the advanced performance of ContrasInver, showing significant superiority in comparison with the current mainstream methods.

C. Application Experiments

This experiment applies ConstraInver to field data, F3 (4 well-logs) and Delft (3 well-logs), both of which are typical of well less surveys. In this experiment, ConstraInver was pre-trained with 5000 steps and semi-supervised training with 50000 steps. Using the AdamW optimizer, the learning rate is 0.001.

1) *F3 Netherlands*: F3 is a very classical survey and many scholars use it for various geophysical and imaging studies [70], such as fault detection [5], [6], salt body detection [4], [71], seismic facies classification [72], seismic denoise [73] and seismic data reconstruction [74]. In which this data is presented in great detail in the work of Alaudah et al [72].

To our knowledge, there are no studies applying it to machine learning-based impedance inversion, mainly because the project with the original F3 survey provided by OpendTect only provides four available impedance logs, which greatly limits the application of machine learning methods to this survey, but ContrasInver has a very few demand for logs, and even using only four or three logs can produce reasonable and reliable results. Fig. 1 shows the F3 survey and the four logs containing the impedance. The OpendTect original project did not provide acoustic impedance logs directly, and the acoustic impedance used for training was obtained from $AI = Vp \times \text{Density}$, where 'Vp' and 'Density' were provided by the original project. For training, we limited the range of acoustic impedance to [3500, 6000], and values greater than 6000 were set to 6000. First we used three logs for training and one log for testing to verify the validity of ConstraInver in the F3 survey, then we used all four logs for training to qualitatively analyze the reliability and reasonableness of the results.

In Fig. 10 (b), we chose a shorter log F02-1 as the validation well-log, and the other three participated in the training. Qualitatively, the figure nicely divides F3 into four well-bounded impedance regions. Among them, ConstraInver accurately predicts the salt-body region with high impedance at the bottom. The middle and lower middle are sands, sandstones, and claystones from Paleocene to Miocene, showing impedance values second only to the saltbody region.

The resulting quantitative metric is visualized in Fig. 11, where we additionally compute the Mean Absolute Percentage

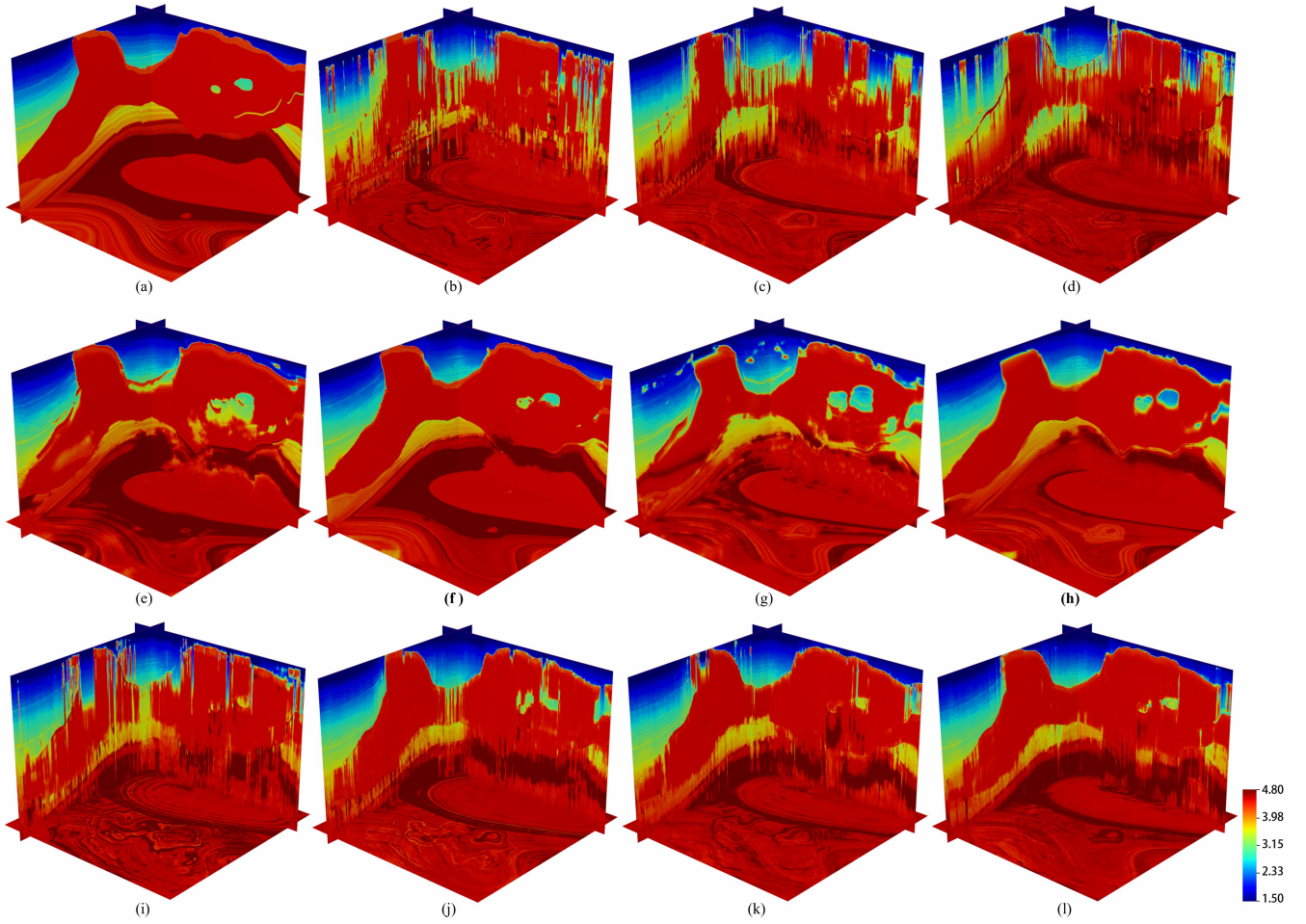


Fig. 8. (b) - (f) training with 9 logs, (g) - (l) training with 4 - 49 logs. (a) Ground truth. (b) ResNet-AE via 9 logs. (c) ResANet-AE via 9 logs. (d) Semi-GAN training via 9 logs. (e) 3D-Pretrain training via 9 logs. (f) ContrasInver training via 9 logs. (g) 3D-Pretrain training via 4 logs. (h) ContrasInver training via 4 logs. (i) ResNet-AE via 16 logs. (j) ResNet-AE via 25 logs. (k) ResNet-AE via 36 logs. (l) ResNet-AE via 49 logs.

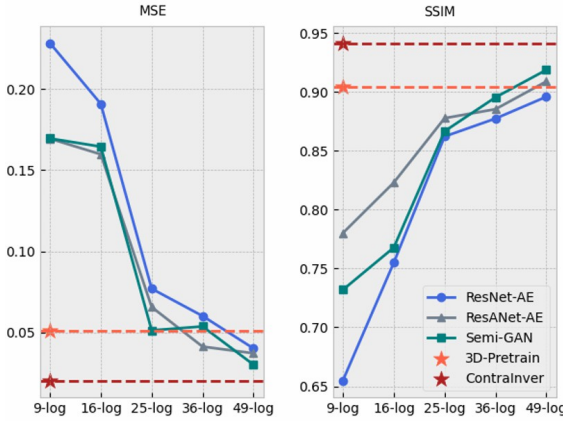


Fig. 9. Variation of quantitative results of 1D-CNN-based method with increasing number of logs.

Error (MAPE) metric on F02-1, MAPE is defined as equation (15).

$$\mathbf{F}_{\text{MAPE}} = \frac{1}{n} \sum_{i=1}^n \left\| \frac{y_i - \hat{y}_i}{y_i} \right\|_1 \times 100\% \quad (15)$$

In field surveys, where impedance orders of magnitude fluctuate widely, MAPE expresses the difference between GT and PV as a ratio to make quantitative results more intuitive. The MAPE of ConstraInver was only 5.079%, indicating that ConstraInver obtained very reliable results with only three well-logs. crossplots also showed a high agreement between the fitted line of ConstraInver and the target line. Fig. 10 (c) shows the results of a four well-logs training, which used all logs for training and therefore was not tested quantitatively, which shows a high similarity to (b). The results shown in the Fig. 10 and 11 are for a purely data-driven approach, without the use of low-frequency constraints [11], which we believe may lead to better results, but are outside the scope of the paper.

2) *Delft*: Delft is still offered as open source by OpendTect [75]. The study survey is located in the West-Netherlands Basin (WNB), a northwest-southeast trending basin along the northeastern margin of the London-Brabant Massif [76]. The survey provided only three well-logs containing acoustic impedance, as shown in Fig. 12.

All three wells are inclined, but this does not affect the application of the 3D method. We used the 'AI final' provided in the original project as the acoustic impedance for training

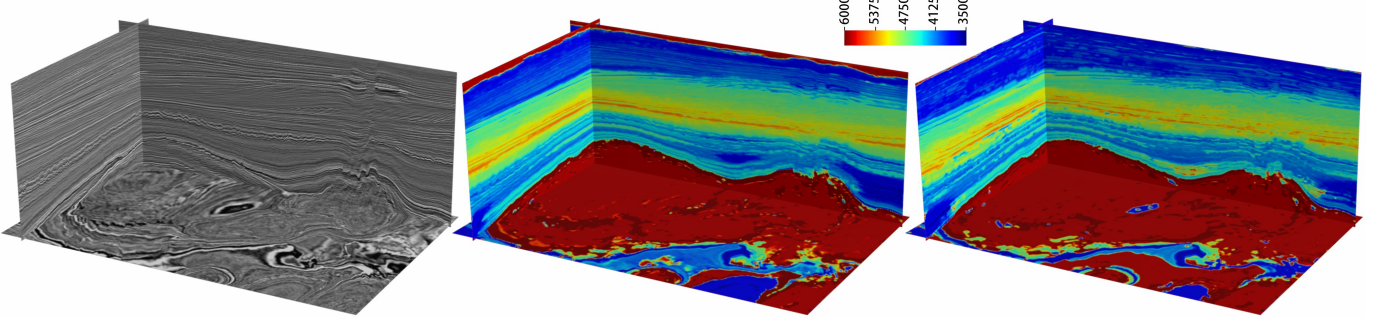


Fig. 10. (a) F3 seismic data. (b) ContrasInver results obtained by training with three well-logs F03-4, F03-2, F06-1 and validating with F02-1. (c) ContrasInver results obtained by training with four well-logs F03-4, F03-2, F06-1 and F02-1.

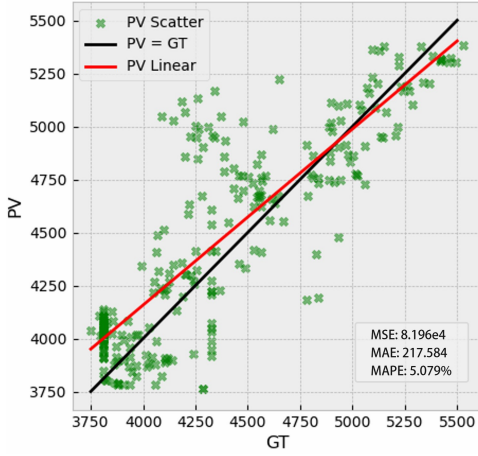


Fig. 11. F3 crossplots of Predictive Value (PV, vertical axis) versus Ground Truth (GT, horizontal axis). The figure shows F02-1, this well-log that was not involved in the training.

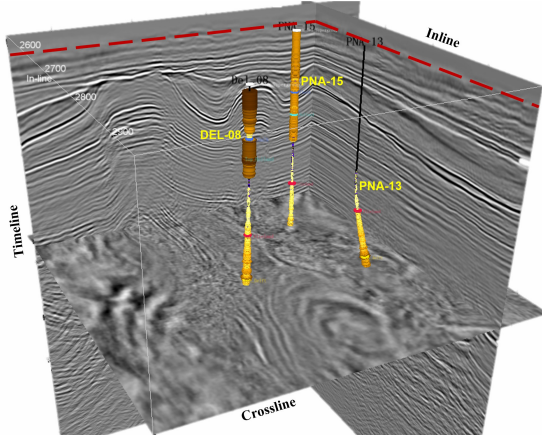


Fig. 12. The figure shows the Delft seismic data along with its three acoustic impedance well-logs, all three of which are inclined wells. This is a typical example of extreme label less.

and validation, with a range of $[3.7e6, 1.5e7]$. First we used two logs for training and one well-log for testing to verify the validity of ContrasInver in the Delft survey, then we used all three well-logs for training to qualitatively analyze the reliability and reasonableness of the results.

In Fig. 13 (b), we chose a shorter log PNA-13 as the

validation well-log, and the other two participated in the training. The ConstraInver-based inversion accurately reflects the trend of the seismic reflection axis, and it clearly captures the abrupt changes in the high-impedance and low-impedance regions at the top of the Delft. The resulting quantitative metric is visualized in Fig. 14. The MAPE of ConstraInver was only 9.802%, indicating that ConstraInver obtained very reliable results with only two well-logs. Crossplots also showed a high agreement between the fitted line of ConstraInver and the target line. Fig. 13 (c) shows the results of a three well-logs training, which used all logs for training and therefore was not tested quantitatively, which shows a high similarity to (b). This result is obtained for a purely data-driven approach.

V. CONCLUSION

In this work, we present ConstraInver, a voxel-wise contrastive semi-supervised learning inversion framework, for the inversion task of 3D seismic data. In ConstraInver, we propose CIPT, LID, VCOR, and design DTKS for improving the training efficiency, verifying the effectiveness of each component through full ablation experiments. In the ablation experiments, we also compare the components in the replacement framework with the currently dominant consistent regularized semi-supervised methods, showing the advantages of our method in quantitative experiments, as well as the very significant improvement in qualitative experiments. The ablation experiments also demonstrate that the projection head has the role of filtering gradient information in the semi-supervision of the regression task, which can significantly improve the performance of the model. In a comparison experiment, we implement three of the current dominant data-driven inversion methods and show that the performance of ConstraInver using nine logs outperforms the performance of the other methods using 49 logs. In the application experiment, we implemented data-driven inversions for two surveys, F3 and Delft, showing the complete inversion profiles and discussing them quantitatively and qualitatively. To the best of our knowledge, this is the first purely data-driven method to perform a full inversion of either F3 or Delft. ConstraInver is a huge advancement for data-driven inversion tasks, allowing learning with an extremely small number of logs and obtaining reasonable and reliable results. Furthermore, it contributes to advances in

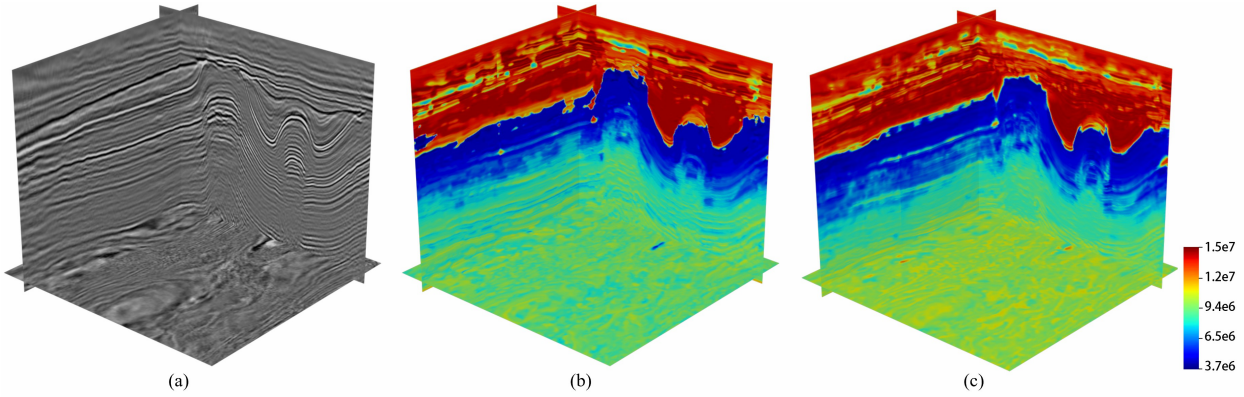


Fig. 13. (a) Delft seismic data. (b) ContrasInver results obtained by training with two well-logs PNA-15, DEL-08 and validating with PNA-13. (c) ContrasInver results obtained by training with three well-logs PNA-15, DEL-08 and PNA-13.

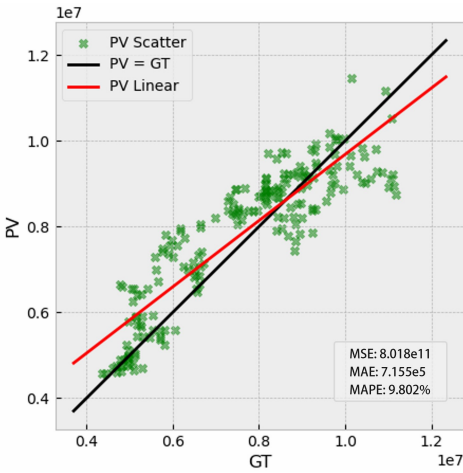


Fig. 14. Delft crossplots of Predictive Value (PV, vertical axis) versus Ground Truth (GT, horizontal axis). The figure shows PNA-13, this well-log that was not involved in the training.

learning theory, especially extending the application of semi-supervised and contrastive learning to regression tasks as well as exploration.

ACKNOWLEDGMENT

The authors are very indebted to the anonymous referees for their critical comments and suggestions for the improvement of this paper. Thanks to Xinming Wu for providing us with the data.

This is a pre-print version of the paper and we will do our best to answer all your questions before the paper is officially published (emindou3015@gmail.com). The code for this paper will be public, and we will subsequently open source it here: <https://github.com/douyimin/ContrasInver>.

REFERENCES

- [1] H. Sun and L. Demanet, “Beyond correlations: Deep learning for seismic interferometry,” *IEEE Transactions on Neural Networks and Learning Systems*, 2022.
- [2] S. Wang, W. Hu, P. Yuan, X. Wu, Q. Zhang, P. Nadukandi, G. O. Botero, and J. Chen, “A self-supervised deep learning method for seismic data deb larding using a blind-trace network,” *IEEE Transactions on Neural Networks and Learning Systems*, 2022.
- [3] N. Iqbal, “Deepseg: Deep segmental denoising neural network for seismic data,” *IEEE Transactions on Neural Networks and Learning Systems*, 2022.
- [4] O. M. Saad, W. Chen, F. Zhang, L. Yang, X. Zhou, and Y. Chen, “Self-attention fully convolutional densenets for automatic salt segmentation,” *IEEE Transactions on Neural Networks and Learning Systems*, 2022.
- [5] Y. Dou, K. Li, J. Zhu, X. Li, and Y. Xi, “Attention-based 3-d seismic fault segmentation training by a few 2-d slice labels,” *IEEE Transactions on Geoscience and Remote Sensing*, vol. 60, pp. 1–15, 2021.
- [6] Y. Dou, K. Li, J. Zhu, T. Li, S. Tan, and Z. Huang, “Md loss: Efficient training of 3-d seismic fault segmentation network under sparse labels by weakening anomaly annotation,” *IEEE Transactions on Geoscience and Remote Sensing*, vol. 60, pp. 1–14, 2022.
- [7] J. Chang, J. Li, Y. Kang, W. Lv, D. Feng, and T. Xu, “Seglog: Geophysical logging segmentation network for lithofacies identification,” *IEEE Transactions on Industrial Informatics*, 2021.
- [8] J. Chang, Y. Kang, W. X. Zheng, Y. Cao, Z. Li, W. Lv, and X.-M. Wang, “Active domain adaptation with application to intelligent logging lithology identification,” *IEEE Transactions on Cybernetics*, 2021.
- [9] R. B. Latimer, R. Davidson, and P. Van Riel, “An interpreter’s guide to understanding and working with seismic-derived acoustic impedance data,” *The leading edge*, vol. 19, no. 3, pp. 242–256, 2000.
- [10] V. Das, A. Pollack, U. Wollner, and T. Mukerji, “Convolutional neural network for seismic impedance inversioncnn for seismic impedance inversion,” *Geophysics*, vol. 84, no. 6, pp. R869–R880, 2019.
- [11] X. Wu, S. Yan, Z. Bi, S. Zhang, and H. Si, “Deep learning for multidimensional seismic impedance inversion,” *Geophysics*, vol. 86, no. 5, pp. R735–R745, 2021.
- [12] D. Meng, B. Wu, Z. Wang, and Z. Zhu, “Seismic impedance inversion using conditional generative adversarial network,” *IEEE Geoscience and Remote Sensing Letters*, vol. 19, pp. 1–5, 2021.
- [13] B. Wu, Q. Xie, and B. Wu, “Seismic impedance inversion based on residual attention network,” *IEEE Transactions on Geoscience and Remote Sensing*, vol. 60, pp. 1–17, 2022.
- [14] Y. Wang, Q. Ge, W. Lu, and X. Yan, “Well-logging constrained seismic inversion based on closed-loop convolutional neural network,” *IEEE Transactions on Geoscience and Remote Sensing*, vol. 58, no. 8, pp. 5564–5574, 2020.
- [15] Y. Wang, Q. Wang, W. Lu, and H. Li, “Physics-constrained seismic impedance inversion based on deep learning,” *IEEE Geoscience and Remote Sensing Letters*, vol. 19, pp. 1–5, 2021.
- [16] Y.-Q. Wang, Q. Wang, W.-K. Lu, Q. Ge, and X.-F. Yan, “Seismic impedance inversion based on cycle-consistent generative adversarial network,” *Petroleum Science*, vol. 19, no. 1, pp. 147–161, 2022.
- [17] Q. Xie, B. Wu, and E. Zhang, “Seismic impedance inversion based on residual attention network,” in *IGARSS 2022-2022 IEEE International Geoscience and Remote Sensing Symposium*. IEEE, 2022, pp. 6153–6156.
- [18] D. Oldenburg, T. Scheuer, and S. Levy, “Recovery of the acoustic impedance from reflection seismograms,” *Geophysics*, vol. 48, no. 10, pp. 1318–1337, 1983.
- [19] L. Wang, Q. Zhao, J. Gao, Z. Xu, M. Fehler, and X. Jiang, “Seismic sparse-spike deconvolution via toeplitz-sparse matrix factorization,” *Geophysics*, vol. 81, no. 3, pp. V169–V182, 2016.

[20] Y. Sui and J. Ma, "A nonstationary sparse spike deconvolution with anelastic attenuation," *Geophysics*, vol. 84, no. 2, pp. R221–R234, 2019.

[21] P. Veeken, D. Silva, and M, "Seismic inversion methods and some of their constraints," *First break*, vol. 22, no. 6, 2004.

[22] X. Wu, "Structure-, stratigraphy-and fault-guided regularization in geophysical inversion," *Geophysical Journal International*, vol. 210, no. 1, pp. 184–195, 2017.

[23] Q. Guo, H. Zhang, H. Cao, W. Xiao, and F. Han, "Hybrid seismic inversion based on multi-order anisotropic markov random field," *IEEE Transactions on Geoscience and Remote Sensing*, vol. 58, no. 1, pp. 407–420, 2019.

[24] M. Bosch, T. Mukerji, and E. F. Gonzalez, "Seismic inversion for reservoir properties combining statistical rock physics and geostatistics: A review," *Geophysics*, vol. 75, no. 5, pp. 75A165–75A176, 2010.

[25] D. P. Hampson, J. S. Schuelke, and J. A. Quirein, "Use of multiattribute transforms to predict log properties from seismic data," *Geophysics*, vol. 66, no. 1, pp. 220–236, 2001.

[26] B. Wu, D. Meng, and H. Zhao, "Semi-supervised learning for seismic impedance inversion using generative adversarial networks," *Remote Sensing*, vol. 13, no. 5, p. 909, 2021.

[27] D. Meng, B. Wu, N. Liu, and W. Chen, "Semi-supervised deep learning seismic impedance inversion using generative adversarial networks," in *IGARSS 2020-2020 IEEE International Geoscience and Remote Sensing Symposium*. IEEE, 2020, pp. 1393–1396.

[28] W. C. Hung, Y. H. Tsai, Y. T. Liou, Y.-Y. Lin, and M. H. Yang, "Adversarial learning for semi-supervised semantic segmentation," in *29th British Machine Vision Conference, BMVC 2018*, 2018.

[29] I. Goodfellow, J. Pouget-Abadie, M. Mirza, B. Xu, D. Warde-Farley, S. Ozair, A. Courville, and Y. Bengio, "Generative adversarial networks," *Communications of the ACM*, vol. 63, no. 11, pp. 139–144, 2020.

[30] M. Ge, W. Zheng, and W. Wang, "Semi-supervised impedance inversion by bayesian neural network based on 2-d cnn pre-training," in *SEG 2021 Workshop: 4th International Workshop on Mathematical Geophysics: Traditional & Learning, Virtual, 17–19 December 2021*. Society of Exploration Geophysicists, 2022, pp. 129–133.

[31] L. Song, X. Yin, Z. Zong, and M. Jiang, "Semi-supervised learning seismic inversion based on spatio-temporal sequence residual modeling neural network," *Journal of Petroleum Science and Engineering*, vol. 208, p. 109549, 2022.

[32] H. Di, X. Chen, H. Maniar, and A. Abubakar, "Semi-supervised seismic and well log integration for reservoir property estimation," in *SEG International Exposition and Annual Meeting*. OnePetro, 2020.

[33] Ö. Çiçek, A. Abdulkadir, S. S. Lienkamp, T. Brox, and O. Ronneberger, "3d u-net: learning dense volumetric segmentation from sparse annotation," in *International conference on medical image computing and computer-assisted intervention*. Springer, 2016, pp. 424–432.

[34] T. Chen, S. Kornblith, M. Norouzi, and G. Hinton, "A simple framework for contrastive learning of visual representations," in *International conference on machine learning*. PMLR, 2020, pp. 1597–1607.

[35] K. He, H. Fan, Y. Wu, S. Xie, and R. Girshick, "Momentum contrast for unsupervised visual representation learning," in *Proceedings of the IEEE/CVF conference on computer vision and pattern recognition*, 2020, pp. 9729–9738.

[36] M. Kaya and H. S. Bilge, "Deep metric learning: A survey," *Symmetry*, vol. 11, no. 9, p. 1066, 2019.

[37] W. Wang, T. Zhou, F. Yu, J. Dai, E. Konukoglu, and L. Van Gool, "Exploring cross-image pixel contrast for semantic segmentation," in *Proceedings of the IEEE/CVF International Conference on Computer Vision*, 2021, pp. 7303–7313.

[38] I. Alonso, A. Sabater, D. Ferstl, L. Montesano, and A. C. Murillo, "Semi-supervised semantic segmentation with pixel-level contrastive learning from a class-wise memory bank," in *Proceedings of the IEEE/CVF International Conference on Computer Vision*, 2021, pp. 8219–8228.

[39] Y. Zhong, B. Yuan, H. Wu, Z. Yuan, J. Peng, and Y.-X. Wang, "Pixel contrastive-consistent semi-supervised semantic segmentation," in *Proceedings of the IEEE/CVF International Conference on Computer Vision*, 2021, pp. 7273–7282.

[40] X. Hu, D. Zeng, X. Xu, and Y. Shi, "Semi-supervised contrastive learning for label-efficient medical image segmentation," in *International Conference on Medical Image Computing and Computer-Assisted Intervention*. Springer, 2021, pp. 481–490.

[41] L.-Z. Guo and Y.-F. Li, "Class-imbalanced semi-supervised learning with adaptive thresholding," in *International Conference on Machine Learning*. PMLR, 2022, pp. 8082–8094.

[42] L. Yang, W. Zhuo, L. Qi, Y. Shi, and Y. Gao, "St++: Make self-training work better for semi-supervised semantic segmentation," in *Proceedings of the IEEE/CVF Conference on Computer Vision and Pattern Recognition*, 2022, pp. 4268–4277.

[43] Y. Zou, Z. Zhang, H. Zhang, C.-L. Li, X. Bian, J.-B. Huang, and T. Pfister, "Pseudoseg: Designing pseudo labels for semantic segmentation," in *International Conference on Learning Representations*, 2020.

[44] S. Zuo, Y. Yu, C. Liang, H. Jiang, S. Er, C. Zhang, T. Zhao, and H. Zha, "Self-training with differentiable teacher," *arXiv preprint arXiv:2109.07049*, 2021.

[45] D.-H. Lee *et al.*, "Pseudo-label: The simple and efficient semi-supervised learning method for deep neural networks," in *Workshop on challenges in representation learning, ICML*, vol. 3, no. 2, 2013, p. 896.

[46] Y. Wang, H. Wang, Y. Shen, J. Fei, W. Li, G. Jin, L. Wu, R. Zhao, and X. Le, "Semi-supervised semantic segmentation using unreliable pseudo-labels," in *Proceedings of the IEEE/CVF Conference on Computer Vision and Pattern Recognition*, 2022, pp. 4248–4257.

[47] E. Arazo, D. Ortego, P. Albert, N. E. O'Connor, and K. McGuinness, "Pseudo-labeling and confirmation bias in deep semi-supervised learning," in *2020 International Joint Conference on Neural Networks (IJCNN)*. IEEE, 2020, pp. 1–8.

[48] S. Mittal, M. Tatarchenko, and T. Brox, "Semi-supervised semantic segmentation with high-and low-level consistency," *IEEE transactions on pattern analysis and machine intelligence*, vol. 43, no. 4, pp. 1369–1379, 2019.

[49] C. S. Perone and J. Cohen-Adad, "Deep semi-supervised segmentation with weight-averaged consistency targets," in *Deep learning in medical image analysis and multimodal learning for clinical decision support*. Springer, 2018, pp. 12–19.

[50] Z. Feng, Q. Zhou, Q. Gu, X. Tan, G. Cheng, X. Lu, J. Shi, and L. Ma, "Dmt: Dynamic mutual training for semi-supervised learning," *Pattern Recognition*, p. 108777, 2022.

[51] Z. Feng, Q. Zhou, G. Cheng, X. Tan, J. Shi, and L. Ma, "Semi-supervised semantic segmentation via dynamic self-training and classbalanced curriculum," *arXiv preprint arXiv:2004.08514*, vol. 1, no. 2, p. 5, 2020.

[52] D. Zhai, B. Hu, X. Gong, H. Zou, and J. Luo, "Ass-gan: Asymmetric semi-supervised gan for breast ultrasound image segmentation," *Neurocomputing*, vol. 493, pp. 204–216, 2022.

[53] Y. Xie, Q. Wan, G. Chen, Y. Xu, and B. Lei, "Retinopathy diagnosis using semi-supervised multi-channel generative adversarial network," in *International Workshop on Ophthalmic Medical Image Analysis*. Springer, 2019, pp. 182–190.

[54] D. Berthelot, N. Carlini, I. Goodfellow, N. Papernot, A. Oliver, and C. A. Raffel, "Mixmatch: A holistic approach to semi-supervised learning," *Advances in neural information processing systems*, vol. 32, 2019.

[55] M. Sajjadi, M. Javanmardi, and T. Tasdizen, "Regularization with stochastic transformations and perturbations for deep semi-supervised learning," *Advances in neural information processing systems*, vol. 29, 2016.

[56] A. Tarvainen and H. Valpola, "Weight-averaged consistency targets improve semi-supervised deep learning results. corr abs/1703.01780," *arXiv preprint arXiv:1703.01780*, vol. 1, no. 5, 2017.

[57] K. Sohn, D. Berthelot, N. Carlini, Z. Zhang, H. Zhang, C. A. Raffel, E. D. Cubuk, A. Kurakin, and C.-L. Li, "Fixmatch: Simplifying semi-supervised learning with consistency and confidence," *Advances in neural information processing systems*, vol. 33, pp. 596–608, 2020.

[58] Q. Xie, Z. Dai, E. Hovy, T. Luong, and Q. Le, "Unsupervised data augmentation for consistency training," *Advances in Neural Information Processing Systems*, vol. 33, pp. 6256–6268, 2020.

[59] A. Tarvainen and H. Valpola, "Mean teachers are better role models: Weight-averaged consistency targets improve semi-supervised deep learning results," *Advances in neural information processing systems*, vol. 30, 2017.

[60] J.-B. Grill, F. Strub, F. Altché, C. Tallec, P. Richemond, E. Buchatskaya, C. Doersch, B. Avila Pires, Z. Guo, M. Gheshlaghi Azar *et al.*, "Bootstrap your own latent-a new approach to self-supervised learning," *Advances in neural information processing systems*, vol. 33, pp. 21271–21284, 2020.

[61] Z. Xie, Y. Lin, Z. Zhang, Y. Cao, S. Lin, and H. Hu, "Propagate yourself: Exploring pixel-level consistency for unsupervised visual representation learning," in *Proceedings of the IEEE/CVF Conference on Computer Vision and Pattern Recognition*, 2021, pp. 16684–16693.

[62] X. Wang, R. Zhang, C. Shen, T. Kong, and L. Li, "Dense contrastive learning for self-supervised visual pre-training," in *Proceedings of the IEEE/CVF Conference on Computer Vision and Pattern Recognition*, 2021, pp. 3024–3033.

[63] F. Liu, X. Qian, L. Jiao, X. Zhang, L. Li, and Y. Cui, "Contrastive learning-based dual dynamic gcn for sar image scene classification," *IEEE Transactions on Neural Networks and Learning Systems*, 2022.

- [64] X. Chen and K. He, "Exploring simple siamese representation learning," in *Proceedings of the IEEE/CVF Conference on Computer Vision and Pattern Recognition*, 2021, pp. 15 750–15 758.
- [65] J. Wang, K. Sun, T. Cheng, B. Jiang, C. Deng, Y. Zhao, D. Liu, Y. Mu, M. Tan, X. Wang *et al.*, "Deep high-resolution representation learning for visual recognition," *IEEE transactions on pattern analysis and machine intelligence*, vol. 43, no. 10, pp. 3349–3364, 2020.
- [66] K. Gupta, T. Ajanthan, A. v. d. Hengel, and S. Gould, "Understanding and improving the role of projection head in self-supervised learning," *arXiv preprint arXiv:2212.11491*, 2022.
- [67] Z. Wen and Y. Li, "The mechanism of prediction head in non-contrastive self-supervised learning," *arXiv preprint arXiv:2205.06226*, 2022.
- [68] I. Loshchilov and F. Hutter, "Decoupled weight decay regularization," in *International Conference on Learning Representations*.
- [69] Z. Wang, A. C. Bovik, H. R. Sheikh, and E. P. Simoncelli, "Image quality assessment: from error visibility to structural similarity," *IEEE transactions on image processing*, vol. 13, no. 4, pp. 600–612, 2004.
- [70] (2020) Project f3 demo 2020. [Online]. Available: <https://terrannubis.com/datainfo/F3-Demo-2020>
- [71] M. A. Shafiq, T. Alshawi, Z. Long, and G. AlRegib, "Salsi: A new seismic attribute for salt dome detection," in *2016 IEEE international conference on acoustics, speech and signal processing (ICASSP)*. IEEE, 2016, pp. 1876–1880.
- [72] Y. Alaudah, P. Michalowicz, M. Alfarraj, and G. AlRegib, "A machine-learning benchmark for facies classification," *Interpretation*, vol. 7, no. 3, pp. SE175–SE187, 2019. [Online]. Available: <https://doi.org/10.1190/INT-2018-0249.1>
- [73] F. Qian, Z. Liu, Y. Wang, Y. Zhou, and G. Hu, "Ground truth-free 3-d seismic random noise attenuation via deep tensor convolutional neural networks in the time-frequency domain," *IEEE Transactions on Geoscience and Remote Sensing*, vol. 60, pp. 1–17, 2022.
- [74] Y. Dou, K. Li, J. Zhu, T. Li, S. Tan, and Z. Huang, "Mda gan: Adversarial-learning-based 3-d seismic data interpolation and reconstruction for complex missing," *arXiv preprint arXiv:2204.03197*, 2022.
- [75] (2021) Project delft. [Online]. Available: <https://terrannubis.com/datainfo/Delft>
- [76] (2019) Dino database. [Online]. Available: <https://www.dinoloket.nl/en>